Supplementary Information

On the water transport mechanism through the microporous layers of operando polymer electrolyte fuel cells probed directly by X-ray tomographic microscopy

Yen-Chun Chen[1], Tim Dörenkamp[1], Christoph Csoklich[1], Anne Berger[2], Federica Marone[3], Jens Eller[1] Thomas J. Schmidt[1,4] and Felix N. Büchi[1]

[1] Electrochemistry Laboratory, Paul Scherrer Institut, 5232 Villigen PSI, Switzerland

[2] Chair of Technical Electrochemistry, Department of Chemistry and Catalysis Research Center, Technical University of Munich, Garching, D-85748 Germany

[3] Swiss Light Source, Paul Scherrer Institut, 5232 Villigen PSI, Switzerland

[4] Laboratory of Physical Chemistry, ETH Zürich, 8093 Zürich, Switzerland

1. Case of well-compensated catalyst shining by image subtraction

With the image alignment process using 3DSlicer 4.11 with parameters described in the Experimental section (2.4), the catalyst shining artifact can be largely mitigated in the case of VGCF-cell as demonstrated in **Figure S1**.
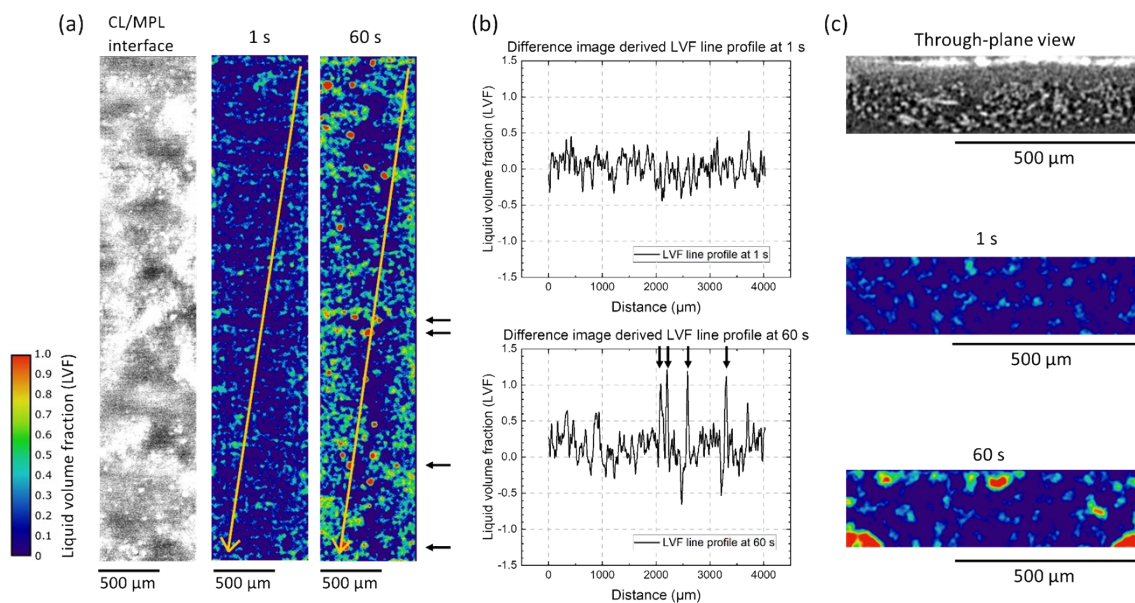

Figure S1 Difference image-derived liquid volume fraction (LVF) distribution of product water at the 1st and 60th second of fuel cell operation demonstrates that catalyst shining can be mitigated by image subtraction. (a) (From left to right) In-plane tomographic image of the CL/MPL interface showing prominent catalyst shining features, 1st second LVF map, 60th second LVF map; (b) LVF line profiles sampled along the respective yellow arrows in (a) with line width = 16 pixels (44 μm) and direction toward bottom left of the images; (c) (from top to bottom) the through-plane view of the MEA at the cathode side, 1st second LVF map, 60th second LVF map.

The liquid volume fraction (LVF) maps are derived from the difference images (see Experimental section 2.4). Shown in **Figure S1a**, at the CL/MPL interface, catalyst shining is

prominent (white blurry features across the whole image). In the LVF map at 1 s, the catalyst shining features are absent due to good image alignment quality. This allows the water distribution to be accurately determined at the CL/MPL interface, as shown in the LVF map at 60 s.

Measuring the line profile of the LVF maps in **Figure S1a** (sampling along the yellow lines in **Figure S1a**), it is seen in the LVF profile at 1 s in **Figure S1b** that the line profile lacks any feature that suggests correspondence to the distribution of catalyst shining features (see the in-plane tomographic image). This proves that catalyst shining artifact is successfully mitigated from the images by image subtraction. Furthermore, shown by the LVF line profile at 60 s, four water droplets were detected along the sampling (yellow) line. Additionally, more positive LVF values are measured, suggesting increased occurrence of liquid water at the CL/MPL interface at 60 s cell operation compared to at 1 s cell operation.

The through-plane LVF images in **Figure S1c** further demonstrates that catalyst shining is well deducted by image subtraction as there is no features in the 1 s through-plane LVF map except for those caused by image noise, and the only features in the 60 s through-plane LVF map are liquid water in the VGCF MPL's larger, ellipsoidal pores or in the channel flow fields.

2. **High frequency resistance of the dry state PEFCs at 90%, 100% and 110% RH conditions**

The dynamic scans (at 1, 3, 5, 10, 15, 30 and 60 s) of the VGCF- and the Li100-cells were done following a drying protocol described in Experimental section 2.2. Towards the end of the drying protocol, humidified hydrogen gas and air were flushed through the VGCF- and the Li100-cells for 20 – 30 s at the anode and cathode, respectively. The high frequency resistance

(HFR) of the PEFCs were recorded for each dry condition at the different inlet gas dew points (43°C, 45°C and 47°C, corresponding to 90%, 100% and 110% RH, respectively). The HFR values were determined by averaging the values of the last 10 s before current jump and are given in **Figure S2**.
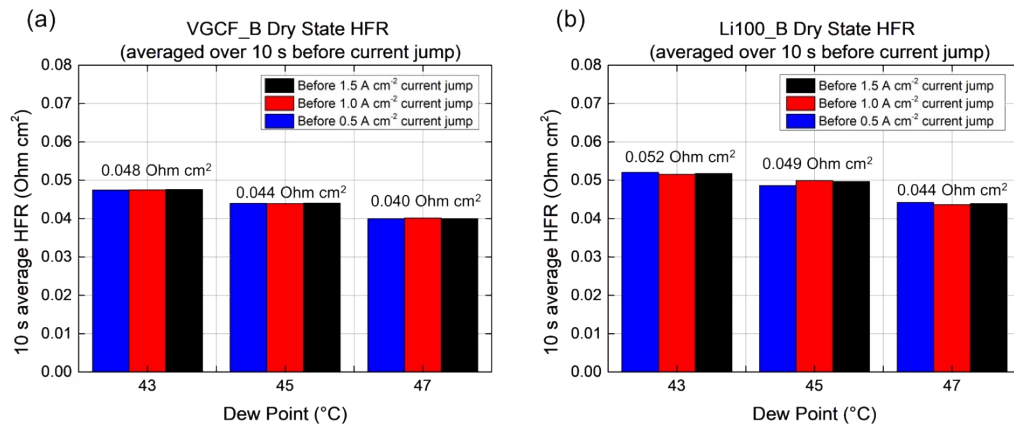

Figure S2 High frequency resistance of the PEFCs before current jump for dynamic scans, shown for the three current density conditions at each dew point (43°C, 45°C and 47°C) (a) for VGCF-cell dry states and the different inlet gas dew points; (b) for Li100-cell dry states at the different inlet gas dew points.

The HFR remains consistent and reproducible for each dew point of the inlet gas for each cell after the drying protocol, and the HFR gradually decreases with increasing dew point, as expected. The difference in HFR between the VGCF- and Li100-cells at the same dew point condition is likely due to different contact resistance among the cell components (CL/MPL/GDL/rib contacts).

It is thus concluded that the drying protocols for the cells are reproducible, and the difference in HFR at different dew point condition for each cell suggests various degree of membrane

hydration, supporting the assumption that dry state differences can be used to simulate the image artifact from membrane swelling, to some extent.

3. VGCF MPL's larger, ellipsoidal pores

The VGCF MPLs come with larger, ellipsoidal pores that are typically 40 – 50 μm wide in the in-plane direction and thinner in the through-plane direction (**Figure S3**).
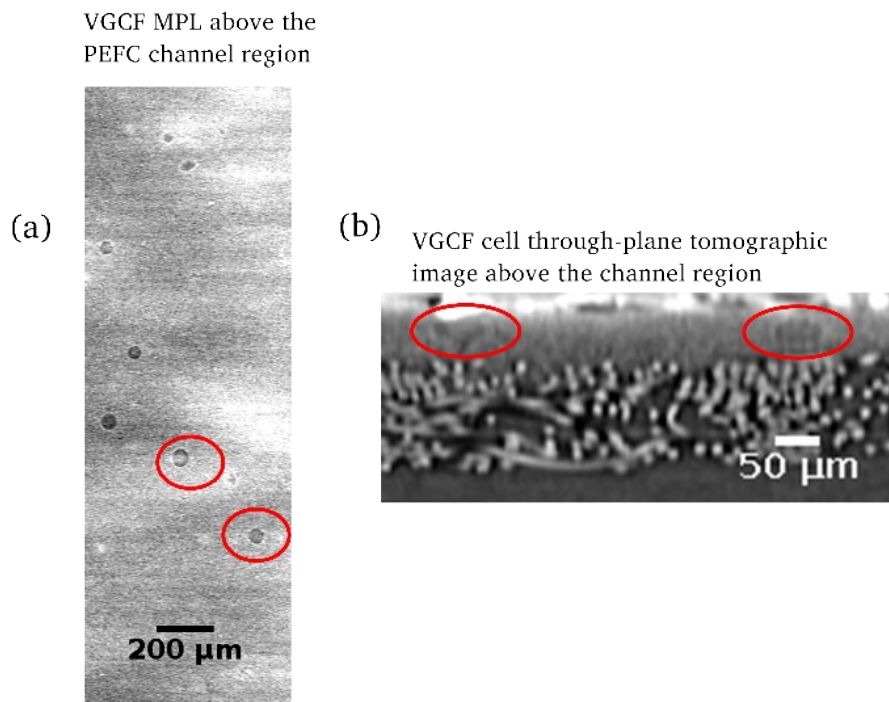

Figure S3 (a) in-plane tomographic image of VGCF MPL (location: above the channel) showing the larger, ellipsoidal pores that are tens of micrometers wide; (b) through-plane image of the CL, VGCF MPL and the H14 GDL substrate. The ellipsoidal pores are marked in red circles.

Note that the greyscale values of these pores are altered by catalyst shining. Therefore, although there is only air in these pores, they appear differently in GSV compared to the void in the GDL substrate.

4. PEFC product water condensation at the rib surface – VGCF-cell

Even at a lower RH condition (90%), when operated at 1.5 A cm^{-2}, a noticeable amount of the water in the VGCF-cell is transported in vapor form. This is demonstrated by the early onset of vapor condensation droplets at 3 s operation time on the VGCF-cell's cathode rib surface (**Figure S4a**). The location of the in-plane tomographic slices in **Figure S4a** is shown in **Figure S4b**.
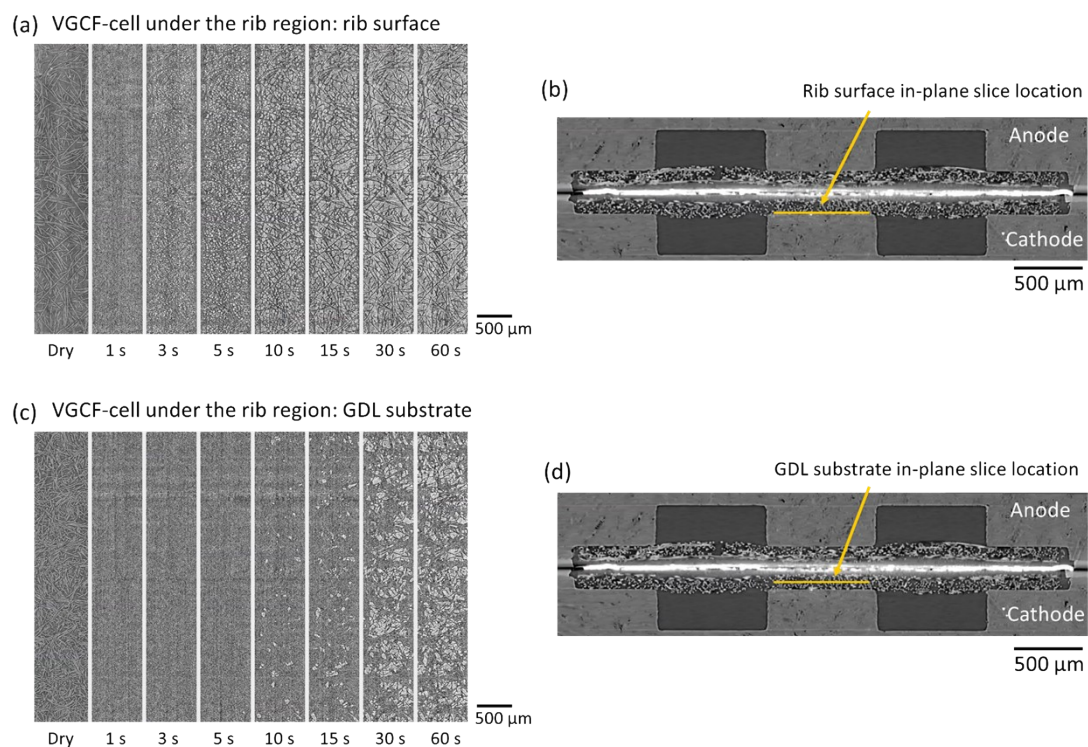
Figure S4 Product water condensation in the rib region of the VGCF-cell operated at 1.5 A/cm^2, 90% RH; (a) greyscale tomographic image of the VGCF-cell rib surface at the dry state and the greyscale difference images of the same location (showing liquid water distribution) at each scanned operation time; (b) location of the rib surface tomographic images in the PEFC; (c) greyscale tomographic image of the VGCF-cell GDL substrate at the dry state and the greyscale difference images of the same location at each scanned operation time; (d) location of the substrate tomographic images in the PEFC.

While noticeable amount of condensed water is observed from 3 s onwards on the rib surface, in the middle part of the GDL substrate, no water is observed until 10 s (**Figure S4c**). The location of the tomographic slices in **Figure S4c** is shown in **Figure S4d**.

This combined observation suggests that water travels in vapor form through the MPL and part of the GDL substrate, and condenses in the substrate pores close to the rib surface, or directly on the rib surface, where the local temperature is lower.

This serves as evidence that during the first few seconds of cell operation, when the water saturation in the GDL substrate is low, vapor condensation instead of capillary fingering is the predominant transport mechanism. It is suspected that capillary fingering processes will take place once the water saturation in the substrate becomes high.

5. Water distribution maps at the CL/MPL interface and in the MPL of the VGCF-cell at all scanned time for 1.5 A/cm^2, 110% RH condition

Liquid water volume fraction distribution maps at all scanned times for VGCF-cell run at 1.5 A/cm^2, 110% RH condition at the CL/MPL interface and in the MPL are shown in **Figure S5**.
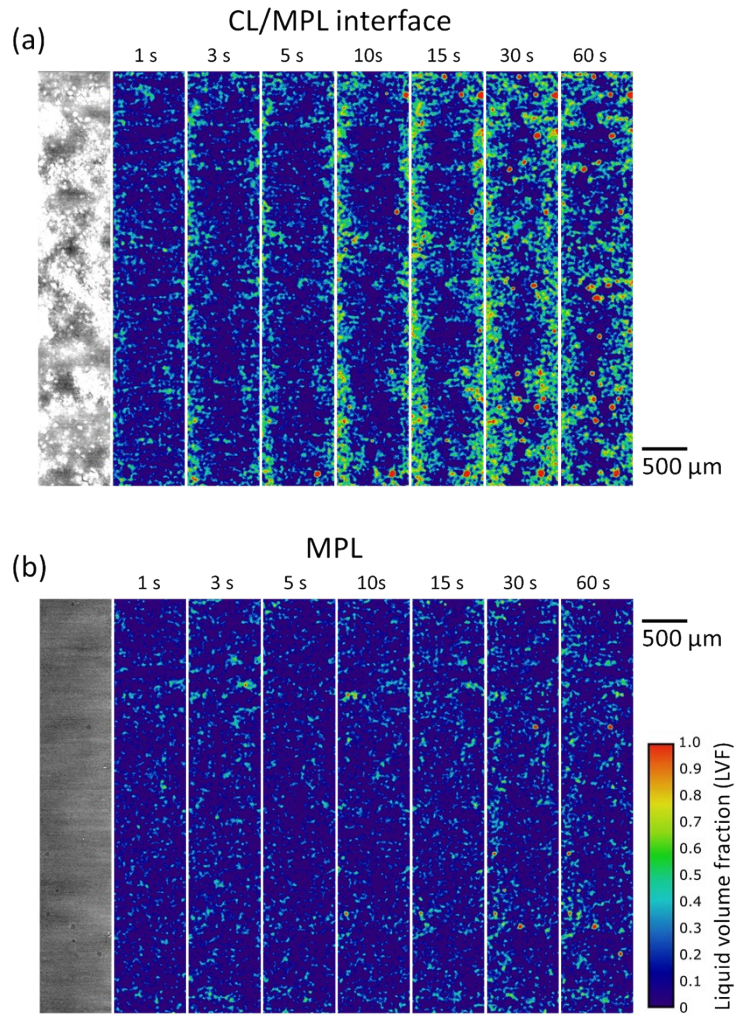
Figure S5 (a) Liquid water volume fraction distribution under the channel (a) at the CL/MPL interface (through-plane position ca. 17 μm in **Figure 4b**) and (b) in the MPL (through-plane position 39 μm), both for the VGCF-cell operated at 1.5 A/cm2 and 110% RH.

6. Compressed Li100 MPL

Though made of carbon black bound by 20 wt% PTFE, the Li100 MPL is observed to be compressed by 42±10% (the error reflects thickness measurement uncertainty) under the rib with respect to under the channel, where the GDL is not compressed (**Figure S6**).
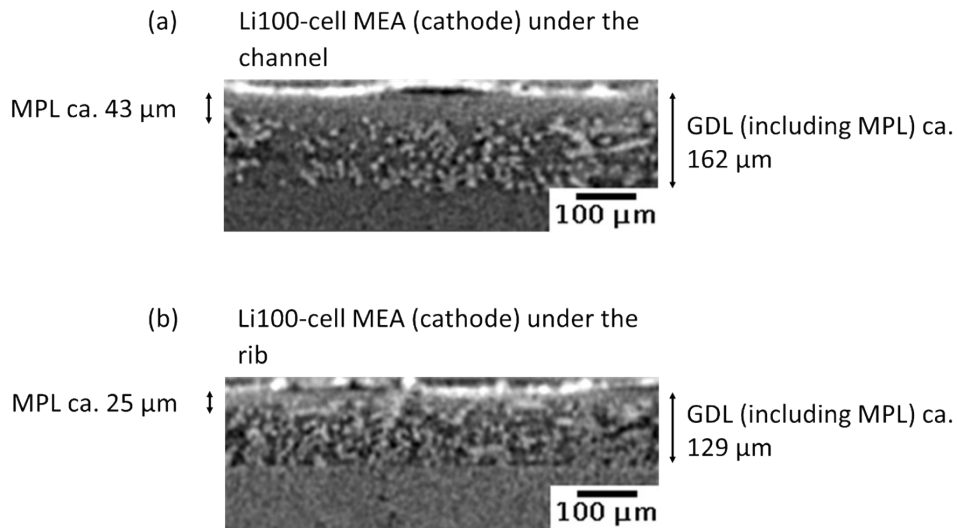
(a)   Li100-cell MEA (cathode) under the channel

MPL ca. 43 µm

GDL (including MPL) ca. 162 µm

100 µm

(b)   Li100-cell MEA (cathode) under the rib

MPL ca. 25 µm

GDL (including MPL) ca. 129 µm

100 µm

Figure S6 Tomographic images of the Li100 MEA (cathode side) (a) under the channel (uncompressed) and (b) under the rib (GDL [including MPL] compressed by 20±3%).

This is a significant compression ratio considering that the total GDL compression (including MPL) is 20±3%. It means that the MPL is subject to higher pressure-induced deformation than the GDL substrate, possibly due to the high porosity (79% when uncompressed).

7. PEFC product water condensation at the rib surface – Li100-cell

The condensation of product water with respect to operation time in the Li100-cell at 0.5 A/cm^2 and 90% RH condition is captured by the difference images (**Figure S7**).
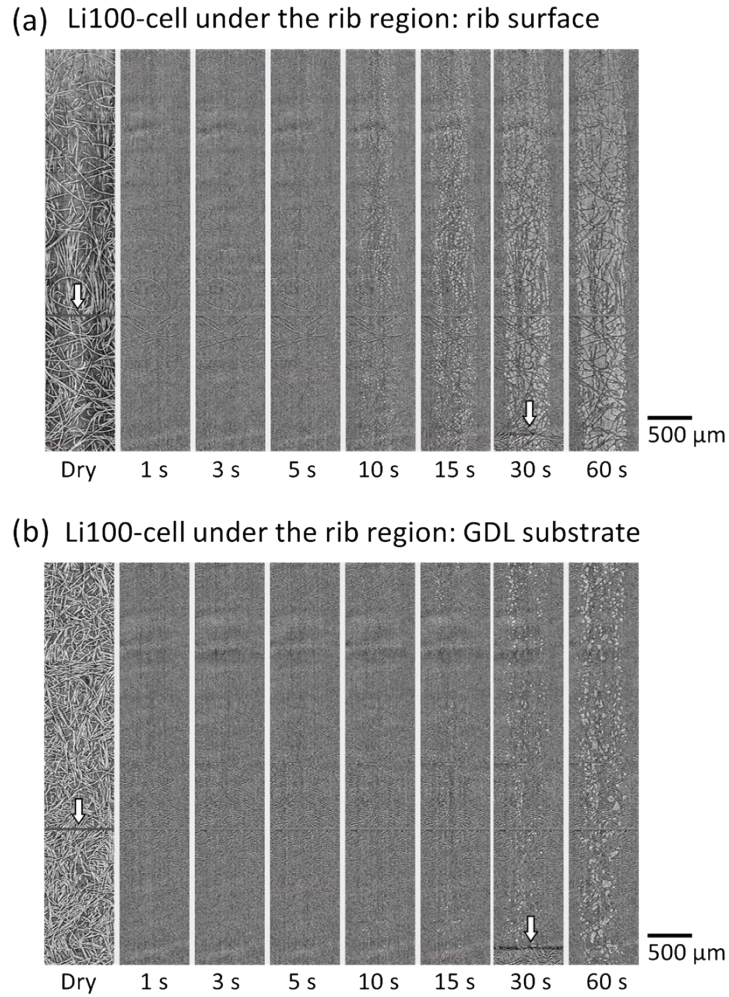
(a) Li100-cell under the rib region: rib surface

Dry   1 s   3 s   5 s   10 s   15 s   30 s   60 s

(b) Li100-cell under the rib region: GDL substrate

Dry   1 s   3 s   5 s   10 s   15 s   30 s   60 s

Figure S7 Product water condensation under the rib region of the Li100-cell operated at 0.5 A/cm^2, 90% RH; (a) greyscale tomographic image of the dry state of the rib surface and the difference images of the same location (showing the liquid water distribution) at each scanned operation time; (b) greyscale tomographic image of the dry state of the GDL substrate and the difference images of the same location at each scanned operation time;

From **Figure S7a** it is seen that condensed water droplets started to form on the Li100-cell rib surface at the 10th second after cell operation and accumulates further until the rib surface is largely filled. On the contrary, in the region close to the middle part of the GDL substrate of the same cell at the same condition, there is less liquid water (**Figure S7b**). Overall, this

suggests predominant vapor transport from the CL to the rib surface at the early stage (the first few seconds) of PEFC operation.

Note that the image alignment quality is compromised around the location where the image data were corrupted (horizontal lines in the images indicated by white arrows in **Figure S7**). This can be seen in the difference images in **Figure S7**, where GDL fiber structures are not aligned in the vicinity of the corrupted region. The reason for data corruption is unclear. Even though the corrupted part is not included in LVF assessment, the evaluation of LVF included parts of the images where GDLs are not fully aligned. It is thus important to probe the influence of image misalignment on the evaluation of averaged LVF.

8. Influence of image misalignment on the evaluation of averaged LVF

Image misalignment hinders the local quantification of liquid water because artificial features (such as those from misaligned GDL fibers) will obscure the real water distribution. However, when evaluating averaged LVF for an image slice with a large amount of pixels (typically > 280,000 pixels in the case of the current study), it was found that the averaged LVF evaluation is insensitive to misalignment that occurs in the in-plane directions. This is because PEFCs components are layered on top of one another and in the in-plane direction, structures tend to repeat themselves. To demonstrate this property and the insensitivity of macroscopic GSV evaluation to in-plane misalignment, a PEFC cathode image stack (CL/MPL/GDL) is duplicated and the duplicated image is translated by (1,1) pixels in-plane. Two images were subtracted and the difference GSVs were measured at each through-plane position (in pixels) in terms of LVF. The result is shown in **Figure S8a**.
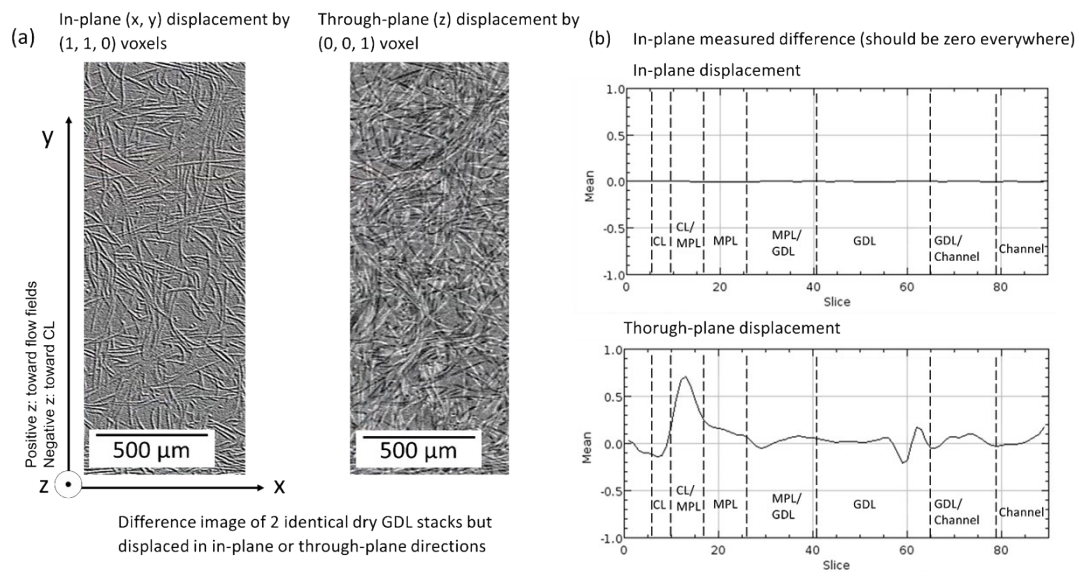
Figure S8 Demonstration of greyscale value differences as a result of in-plane (IP) cathode (CL, MPL and GDL) structural misalignment and through-plane (TP) structural misalignment; (a) Greyscale difference images of the two identical structures displaced by a short distance in-plane or through-plane; (b) the resultant GSV difference across the GDL through-plane slices.

From **Figure S8a**, it is seen that in-plane misalignment by (1,1) pixels does not alter the average LVF measurement, since the different layers (CL, MPL and GDL) tend to repeat their structures in these directions and in-plane displacement alters only minorly the total amount of materials in the measured region.

However, in the through-plane direction, PEFC components' structures change significantly, especially at the interfacial regions. Misalignment in the through-plane directions causes drastic error in the LVF estimation, as shown in **Figure S8b**. The intensity peak at slice 10 to 15 shows particularly pronounced error at the CL/MPL interface caused by the sudden change in X-ray attenuation coefficients across the CL and MPL. Membrane swelling-induced artifact is also a result of through-plane misalignment.

9. MPL LVF discernability derived from Gaussian-distributed image noise

The 2.8σ discernability criterion corresponds to 95% confidence. On an LVF image with image noise of magnitude σ, select two regions of a definite area, if the average LVF difference between these two regions is >2.8σ, there is 95% confidence that the difference cannot be just a result of image noise. Hence, once the average LVF difference of two regions is >2.8σ, it is judged that these two regions have different physical LVF (=actual LVF).

For the mean-filtered operando LVF images of the PEFC based on 0.8 s scans (the dynamic scans), the 2.8σ discernability with respect to number of averaged voxels is provided in **Figure S9**.
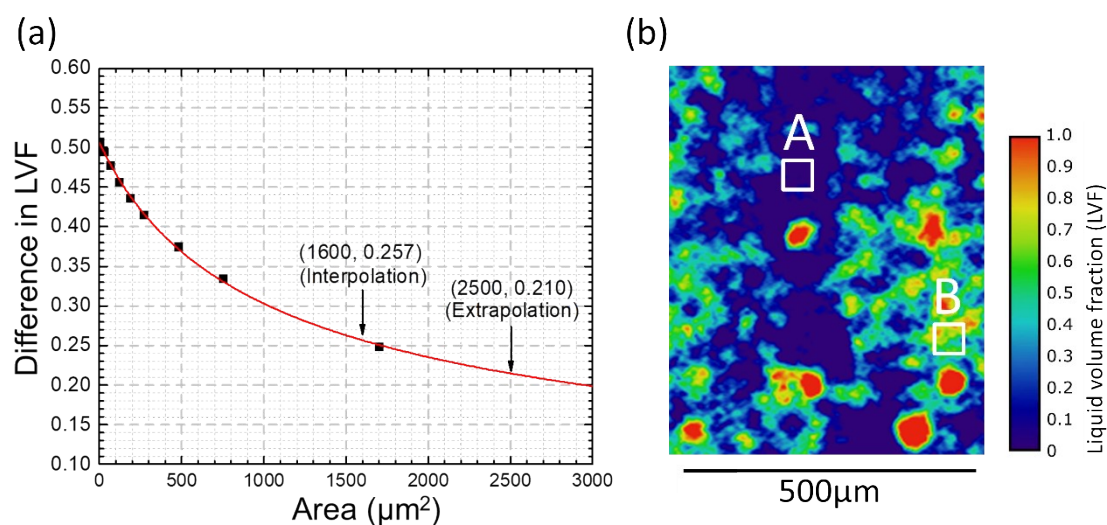

Figure S9 (a) 2.8σ liquid volume fraction (LVF) discernability with respect to sampled area over which average LVF is taken (95% confidence); (b) a LVF map where the discernability curve can be applied: each squared region is 50 μm × 50 μm (2500 μm²) in area, corresponding to discernability of 0.210 in LVF.

The fitted discernability curve (red curve in **Figure S9**) has an exponent of -0.52, close to the predicted behavior of Gaussian-distributed image noise with respect to size of average. This curve allows us to interpret the LVF images despite image noise. For example, when interpreting the LVF maps of **Figure 5**, suppose the image artifacts are negligible there and the fitting curve can be extrapolated, then any regions of 2500 μm^2 area having average LVF differing among one another by >0.21 LVF can be judged to have different physical LVF in those regions.

For example, the discernability curve in **Figure S9a** is applicable to **Figure S9b**. Since the squared region in A has a LVF more than 21% less than the region in B, these two regions can be judged—in the absence of image artifacts—to have different physical LVF on average.